Editors' Suggestion

Erasure Detection of a Dual-Rail Qubit Encoded in a Double-Post Superconducting Cavity

Akshay Koottandavida,[*,†] Ioannis Tsioutsios,[*,‡] Aikaterini Kargioti, Cassady R. Smith, Vidul R. Joshi, Wei Dai, James D. Teoh, Jacob C. Curtis, Luigi Frunzio, Robert J. Schoelkopf, and Michel H. Devoret[§]

Department of Applied Physics, Yale University, New Haven, Connecticut 06520, USA and Yale Quantum Institute, Yale University, New Haven, Connecticut 06511, USA

(Received 17 November 2023; accepted 3 April 2024; published 2 May 2024)

Qubits with predominantly erasure errors present distinctive advantages for quantum error correction (QEC) and fault-tolerant quantum computing. Logical qubits based on dual-rail encoding that exploit erasure detection have been recently proposed in superconducting circuit architectures, with either coupled transmons or cavities. Here, we implement a dual-rail qubit encoded in a compact, double-post superconducting cavity. Using an auxiliary transmon, we perform erasure detection on the dual-rail subspace. We characterize the behavior of the code space by a novel method to perform joint-Wigner tomography. This is based on modifying the cross-Kerr interaction between the cavity modes and the transmon. We measure an erasure rate of $3.981 \pm 0.003\ (\mathrm{ms})^{-1}$ and a residual, postselected dephasing error rate up to $0.17\ (\mathrm{ms})^{-1}$ within the code space. This strong hierarchy of error rates, together with the compact and hardware-efficient nature of this novel architecture, holds promise in realizing QEC schemes with enhanced thresholds and improved scaling.

DOI: 10.1103/PhysRevLett.132.180601

Introduction.—Quantum error correction (QEC), the process of protecting quantum information from decoherence, is an essential ingredient toward fault-tolerant quantum computation (FTQC). QEC involves redundantly encoding logical qubits into an enlarged Hilbert space, targeting coherence that significantly exceeds that of its constituent components. QEC codes can be roughly categorized into discrete variable codes [1], such as the surface code [2–4], or continuous variable codes, such as the Gottesman-Kitaev-Preskill [5], binomial [6], or cat codes [7,8]. Experimentally, bosonic QEC codes have proven to be efficient in reducing error rates on the single logical-qubit level [9–11], while discrete variable codes have demonstrated suppression of logical error rates by increasing code distance [12]. Hence, combining the two approaches where error-corrected bosonic qubits form the base layer of surface code architectures may be a promising pathway toward FTQC.

Alternatively, recent studies have shown that systems with an erasure noise channel at the base layer can reduce the logical error rate by substantially increasing both the threshold and distance of the outer surface code [13,14]. Erasures are leakage errors to outside the computational subspace that are detected in real time and for which the physical qubits that were impacted are also located in space. Qubits predominantly subject to erasures, so-called "erasure qubits," have been proposed with metastable states of neutral atoms [14–16] and dual-rail qubits based on superconducting circuit quantum electrodynamics (cQED) architecture [17,18]. While the dual-rail encoding has been a subject of extensive study in the quantum optics platform [19] and has been investigated in superconducting circuits [20–22], it has only recently been implemented in cQED systems in the context of erasure errors [23,24].

A successful incorporation of erasure qubits into a QEC architecture requires a system that exhibits strong hierarchy of errors [14]. This means that the dominant errors are converted to erasures and the remaining Pauli and leakage errors exhibit orders of magnitude lower rates. To this end, superconducting cavity modes are ideal candidates to encode a dual-rail erasure qubit, since they present natural noise bias, with photon loss being the dominant error mechanism [18,24]. In addition, superconducting cavities, especially those implemented in 3D geometries, exhibit longer lifetimes with lower intrinsic dephasing rates compared to transmons. Nonetheless, the nonlinearity of auxiliary transmons is still a necessary ingredient for the control of cavity modes. As a result, dual-rail qubits with cavity modes suffer from additional loss channels introduced by these nonlinear elements.

In this Letter, we present a dual-rail qubit implemented in a hardware-efficient, 3D cavity architecture—the symmetric and antisymmetric eigenmodes of a double-post coaxial superconducting aluminum cavity. The highly delocalized field distributions of the modes allow for a compact architecture in which a single, dispersively coupled auxiliary transmon provides the necessary nonlinearity for state preparation, erasure detection, and tomography. Hence, compared to other approaches [24], our architecture requires fewer resources. By modifying the dispersive

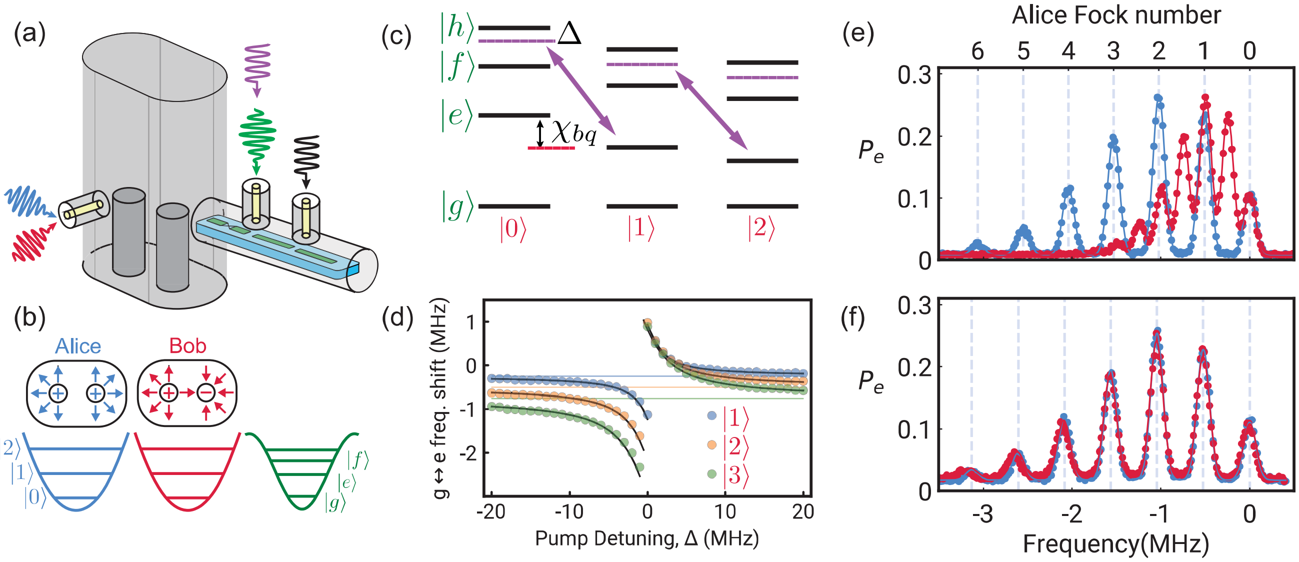

FIG. 1. (a) Schematic of the double-post cavity, made of 5N aluminum with a transmon qubit, readout, and Purcell filter fabricated on a sapphire chip. (b) Field distributions of the symmetric (Alice) and antisymmetric (Bob) eigenmodes of the system, encoding the dual-rail qubit. (c) Energy-level diagram of the combined Bob-transmon system showing dispersive shifts. The purple arrows connect the pairs of levels $|n-1,h\rangle$ and $|n,e\rangle$ being coupled via the cross-Kerr tuning drive. (d) Avoided crossing observed when preparing $|n,e\rangle$ states in Bob-transmon, sweeping pump detuning Δ with fixed amplitude $\Omega/2\pi = 0.5$ MHz. No drive is applied to affect Alice-transmon coupling. Solid horizontal lines are a visual aid to the bare Fock state energies, and simulation results are overlaid in black lines. (e) Number-split peaks of the transmon when either Alice (blue) or Bob (red) is populated with a coherent state of amplitude $\alpha = 1.5$, without any pump. (f) Bob's peaks align with that of Alice in the presence of the cross-Kerr tuning pump with parameters $(\Omega/2\pi, \Delta/2\pi) = (0.5, -5.4)$ MHz.

interaction between the cavity modes and the transmon [25], we perform joint-Wigner tomography on the two modes to characterize the erasure detection circuit. We show that our quantum nondemolition (QND) erasure detection scheme converts cavity photon losses to erasures with a false-negative probability of only 0.28% per gate. We demonstrate a strong hierarchy of error rates with erasures occurring at a rate of $3.981 \pm 0.003\ (\mathrm{ms})^{-1}$ and postselected Pauli $\hat{Z}$ errors at a rate of up to $0.170\ (\mathrm{ms})^{-1}$. Moreover, postselected bit-flip or Pauli $\hat{X}$ type errors occur at a negligible rate of $\sim 10^{-4}\ (\mathrm{ms})^{-1}$. These results demonstrate the viability of incorporating such an erasure detection scheme in a circuit (so-called midcircuit erasure detection) and, consequently, use the dual-rail as an erasure qubit in concatenation codes to enhance QEC thresholds.

Experimental system.—Figure 1(a) depicts our experiment, which comprises a coaxial superconducting cavity made of high-purity (5N) aluminum [26] with two posts of equal length. The package hosts two modes, Alice ($\hat{a}$) and Bob ($\hat{b}$), which are the harmonic oscillators used to encode the dual-rail qubit. An auxiliary transmon fabricated on a sapphire chip is inserted into the package [27–30] (see Supplemental Material [31] for full system parameters). The delocalized electromagnetic field distribution of Alice and Bob [Fig. 1(b)] creates coupling to the transmon with similar strengths. This leads to a static dispersive interaction:

$$\hat{H}/\hbar = \chi_{aq}\hat{a}^\dagger\hat{a}|e\rangle\langle e| + \chi_{bq}\hat{b}^\dagger\hat{b}|e\rangle\langle e| \tag{1}$$

with measured cross-Kerr rates $\chi_{aq}/2\pi = -0.514$ MHz and $\chi_{bq}/2\pi = -0.251$ MHz. This coupling enables our erasure detection scheme. However, the residual mismatch in cross-Kerr rates renders tomography in the combined Hilbert space a rather challenging task [32,33].

Cross-Kerr matching.—The motivation behind matching the cross-Kerr rates in Eq. (1) is to perform joint-Wigner tomography on the combined Hilbert space of Alice and Bob. The joint-Wigner function [34] given by

$$W(\alpha,\beta) = \frac{4}{\pi^2}\mathrm{Tr}[\hat{D}(-\alpha,-\beta)\rho\hat{D}(\alpha,\beta)\hat{\Pi}] \tag{2}$$

requires the measuring the expectation value of the joint-parity operator:

$$\hat{\Pi} = (-1)^{\hat{a}^\dagger\hat{a}+\hat{b}^\dagger\hat{b}} \tag{3}$$

of the displaced state. If $\chi_{aq} = \chi_{bq} = \chi$, this measurement is greatly simplified via a Ramsey-like sequence [Fig. 2(b)], similar to the single-mode Wigner tomography. By choosing the wait time such that $t_W = \pi/\chi$, the joint parity is mapped on to the transmon states (see Supplemental Material [31]). To match the cross-Kerr rates, we leverage the four-wave mixing property of the transmon [25] and

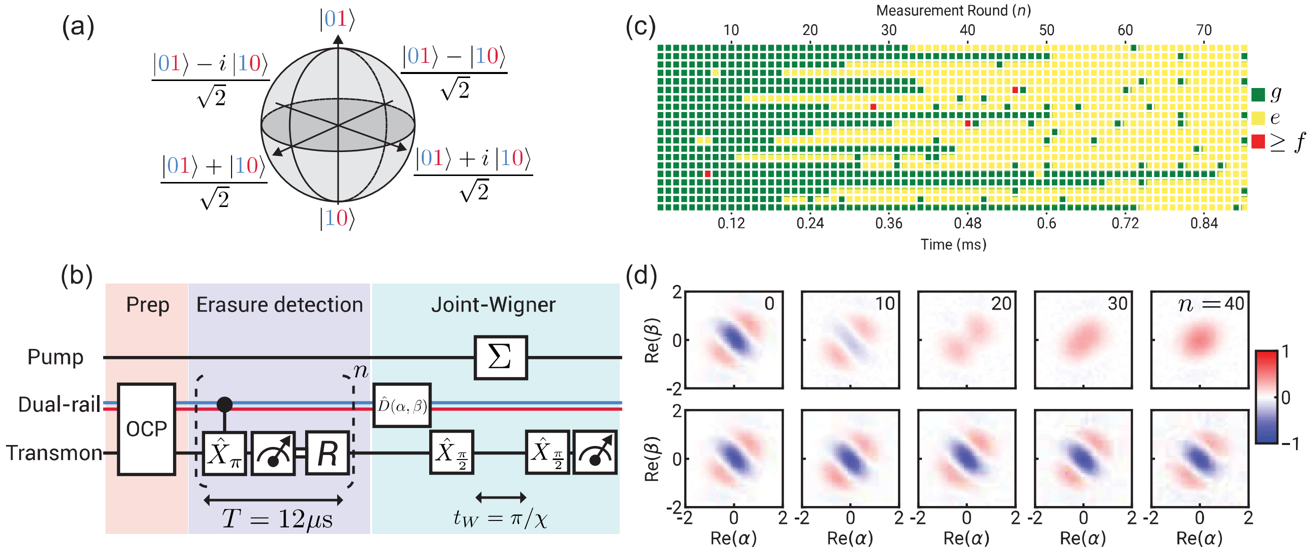

FIG. 2. (a) Dual-rail Bloch sphere where the code words are two-mode Fock states $|+Z\rangle_L = |01\rangle$ and $|-Z\rangle_L = |10\rangle$ (the first mode is Alice, and the second mode is Bob). (b) Erasure detection using a selective π pulse centered at the transmon frequency ($\hat{X}^0_\pi$). After n detection rounds, we perform joint-Wigner tomography on the system with the cross-Kerr matched Hamiltonian $\hat{H}_\Sigma$ represented as the Σ gate. (c) Experimental results of erasure detection for $n = 75$ rounds after preparing the $|+X\rangle_L$ state. Each row is an separate run of the circuit. Ideally, state transition from $|g\rangle \to |e\rangle$ heralds an erasure for the dual-rail qubit. But readout infidelities and transmon errors cause deviation from this behavior in the form of isolated "e" or "f" outcomes. (d) Experimental result of the full circuit shown in (b). Erasure detection is performed on the $|+X\rangle_L$ state for n rounds before measuring the Re(α)-Re(β) joint-Wigner cut of the state. The experiment is repeated for $n = 0$, 10, 20, 30, 40 rounds. The initial state clearly decays to the ground state due to cavity photon loss. Postselecting on a qubit being in "g" in the trajectory data, we can reconstruct the encoded information, visually proving faithful conversion of photon loss to erasures.

apply a microwave drive at frequency $\omega_\chi = \omega_{he} - \omega_b + \Delta$, with amplitude Ω. This process exchanges two photons from the transmon with one photon each from the drive and one of the cavities, coupling pairs of levels $|n, e\rangle \leftrightarrow |n-1, h\rangle$. Here, $|n\rangle$ denotes the nth Fock state of the relevant cavity mode, and $|e\rangle$ and $|h\rangle$ represent the first and third excited states, respectively, of the transmon. By detuning the pump by Δ, we shift the energy levels of the Fock states from their bare values. In the $\chi \ll \Omega \ll \Delta$ regime, this can be approximated as a change in the cross-Kerr rate between the modes [Fig. 1(c)].

For the purposes of this Letter, we choose to tune only χ_{bq} and keep χ_{aq} constant. We opted to match to the higher cross-Kerr rate of Alice in order to achieve faster gate times. This independent control of the cross-Kerr rates is possible due to the large detuning (≈200 MHz) between the cavity modes. The avoided crossings in Fig. 1(d) reveal the tuning of the energy levels of the Bob-transmon system due to the pump. We then set pump parameters (Ω, Δ) such that the cross-Kerr rates are matched. To confirm cross-Kerr matching, we perform spectroscopic measurements on the transmon after preparing a coherent state in either cavity mode. Figures 1(e) and 1(f) show the effect of the pump on the number split peaks [35] of the cavities, where Bob's peaks align with those of Alice. Hence, we can approximate the interaction Hamiltonian as

$$\hat{H}_\Sigma/\hbar \approx \chi(\hat{a}^\dagger\hat{a} + \hat{b}^\dagger\hat{b})|e\rangle\langle e| \tag{4}$$

up to six Fock states. The extracted pumped cross-Kerr rates were $\chi_{aq}/2\pi = -0.521$ MHz and $\chi_{bq}/2\pi = -0.527$ MHz. We note that by increasing the pump amplitude Ω we can potentially tune higher Fock states as well.

Erasure detection.—The dual-rail qubit is defined in the joint Hilbert space of Alice and Bob with $|+Z_L\rangle = |01\rangle$ and $|-Z_L\rangle = |10\rangle$ as the logical code words [Fig. 2(a)]. The dominant error channel in superconducting 3D cavity modes is single-photon loss. Photon losses in either Alice or Bob destroy the logical dual-rail encoding and leave the system in the error state $|00\rangle$. In our system, these errors occur at rates $\kappa_a = 4.454 \pm 0.044$ (ms)$^{-1}$ ($T_1^a = 224.5 \pm 2.2$ μs) and $\kappa_b = 3.339 \pm 0.018$ (ms)$^{-1}$ ($T_1^b = 299.4 \pm 1.6$ μs) for Alice and Bob, respectively. To detect photon losses, we leverage the dispersive interaction between the cavity modes and the transmon [Eq. (1)]. After initializing the system in the code space, we query the transmon state using a frequency selective pulse centered at its bare frequency (ω_{ge}). The transmon state flips only when the cavity modes are in $|00\rangle$ (error space). Our circuit to realize this is shown in Fig. 2(b). We prepare the states in the code space via optimal control pulses (OCP) [36–38], and the transmon is initialized in its ground state ($|g\rangle$). The selective pulse to flip the transmon state is a long ($4\sigma = 8$ μs) Gaussian pulse ($\hat{X}_\pi$). This is followed by a readout and a fast reset of the transmon state to $|g\rangle$. The entire circuit takes exactly 12 μs to execute and should output readout result e if the cavity modes are in the error space and g otherwise.

Figure 2(c) displays the results of performing erasure detection for $n = 75$ rounds on the $|+X_L\rangle = (1/\sqrt{2})(|01\rangle + |10\rangle)$ state. Each row in the plot represents a different experimental shot. The first row depicts a near-ideal trajectory where the transmon state remains in $|g\rangle$ until measurement round 32. Because of a photon loss event in either cavity, the transmon frequency shifts to its bare value, causing the $\hat{X}_\pi$ gate to flip its state to $|e\rangle$. The transmon remains in this state for the remainder of the time due to the reset operation. Nonidealities arising from readout inefficiencies and transmon errors, however, cause many trajectories to deviate from the ideal behavior. To characterize the erasure detection circuit under these errors, we feed the raw trajectories to a hidden Markov model. The model learns a state transition matrix, describing the probability of transitions between code space and error space at each time step, and an emission matrix, which predicts the probability of an outcome (g/e) given a hidden state. From this model, we extract a false-negative probability, defined as the probability of misassigning an erasure as being within the code space, of 0.28% per measurement. Additionally, we extract a $> 99.9\%$ measure of QND on the cavity photon number, for our detection scheme. This means that the erasure detection itself induces minimal backaction compared to having no detection. This is a crucial feature for incorporating such erasure checks in a surface code. Finally, we note that each erasure check accrues a deterministic phase on superpositions of states in the dual-rail subspace. In the experiment, we calibrate this and apply software corrections to the tomography pulses to cancel it.

Joint tomography.—To determine the behavior of the code space during detection, we perform direct tomography on the cavities. Since the dual-rail code is defined in the joint Hilbert space of Alice and Bob, we measure the joint-Wigner function [32], using the circuit shown in Fig. 2(b). During the waiting time (t_W), we establish the cross-Kerr matched interaction Hamiltonian by applying the pump with the matching parameters, thereby measuring the expectation value of the joint-parity operator. Note that the joint-Wigner function is defined in a 4D space, since α and β are complex numbers, representing position and conjugate momentum variables of each mode. As a result, it is challenging to visualize and would require an exponential number of samples to characterize accurately.

Instead, to efficiently characterize the system, we perform partial tomography by sparsely sampling the values of (α, β). First, to visually verify the evolution of the states during erasure detection, we measure a 2D cut of the full joint-Wigner space, specifically the $\mathrm{Re}(\alpha)$-$\mathrm{Re}(\beta)$ cut with $\mathrm{Im}(\alpha) = \mathrm{Im}(\beta) = 0$. In the top row in Fig. 2(d), we observe the evolution of the $|+X_L\rangle$ state after $n = 0, 10, 20, 30, 40$ rounds of erasure detection. As expected, the state eventually decays to the error space $|00\rangle$. After discarding trajectories where erasures were detected, we are clearly able to recover the original information [Fig. 2(d), bottom panel]. This improvement comes at the expense of discarding more data as we track the system for longer times. Since we are measuring only a cut of the joint Wigner, we have only partial information about the system, and it is not enough to reconstruct the full density matrix.

Having visually confirmed that our erasure detection scheme enables faithful recovery of the encoded information, we proceed to quantify how good our detection scheme is. To achieve this, we measure the logical Pauli state vector components for the dual-rail subspace after preparing in the six cardinal states of the Bloch sphere. This measurement is performed using the same circuit as before [Fig. 2(b)]. By projecting the joint-Wigner function in Eq. (2) onto the dual-rail subspace, we extract the expectation values of the Pauli operators by sampling only 16 points (α_i, β_i) in phase space (see Supplemental Material [31]) [32,33].

Figure 3(a) illustrates the decay of the expectation values of the four Pauli operators, $(\hat{I}, \hat{X}, \hat{Y}, \hat{Z})$, for different states on the Bloch sphere, as a function of the number of detection rounds. The expectation values decay exponentially due to the single-photon loss channels. Crucially, we observe the decay of the identity operator $(\hat{I})$, indicating that the system decays outside the code space. Averaged over the six cardinal states on the Bloch sphere, we obtain an erasure rate of $3.981 \pm 0.003\ (\mathrm{ms})^{-1}$ or 4.8% per measurement.

Discarding the trajectories where an erasure was detected, we extract residual Pauli error rates, within the code space. The $\hat{I}$ and the $\hat{Z}$ operator expectation values are nearly constant, and we are able to provide an upper bound on their decay rates of only $\sim 10^{-4}\ (\mathrm{ms})^{-1}$. The postselected $\hat{X}$ and $\hat{Y}$ operators exhibit no-jump evolution, i.e., the conditional update of the density matrix of the system upon measuring no photon jumps [24]. For the dual-rail qubit, this effect causes any superposition of states to deterministically decay toward the cavity with lower decay rate (in our case, Bob). In principle, it is possible to exactly cancel this effect by designing modes with equal decay rates or by interleaving SWAP operations between the cavities such that the photon spends equal amounts of time in each mode [18]. Fitting this deterministic no-jump evolution, we extract residual dephasing rates up to $0.170\ (\mathrm{ms})^{-1}$ ($\approx 0.2\%$ per measurement). Note that we are discarding exponentially many trajectories as we perform erasure detection for more rounds, as seen in the survival probability plot in Fig. 3(b), which shows the number of trajectories that survive as a function of detection rounds.

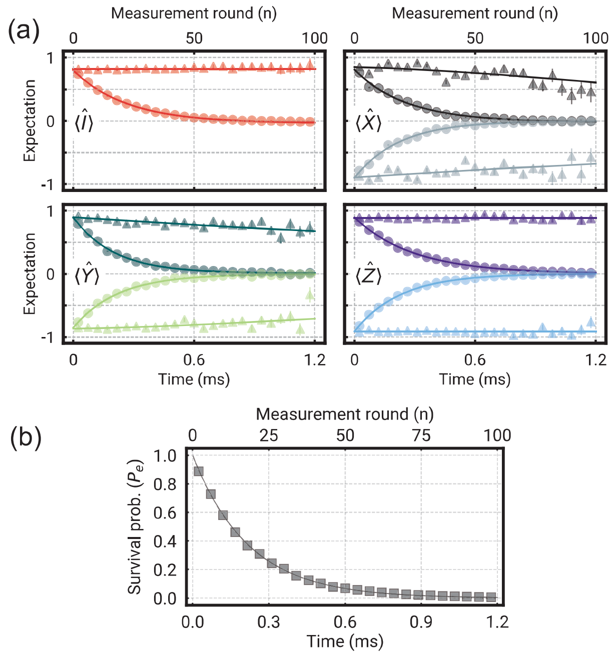

FIG. 3. (a) Expectation values of the logical Pauli operators $\hat{I}$, $\hat{X}$, $\hat{Y}$, and $\hat{Z}$ for the dual-rail subspace as a function of detection rounds, measured using the circuit in Fig. 2(b). Triangles indicate data after postselecting on no erasures from the dots. For $\langle\hat{X}\rangle$, the experiment is performed after preparing the $|+X\rangle$ (darker color at the top) and $|-X\rangle$ (lighter color at the bottom) states. The same is repeated for $\langle\hat{Y}\rangle$ and $\langle\hat{Z}\rangle$. Postselection preserves the expectation values for far longer. The fits (shown in solid lines) for the postselected data account for the no-jump evolution, due to the difference in lifetimes between Alice and Bob, and residual Pauli errors within the subspace. (b) Survival probability, i.e., the fraction of experimental shots that survive after n rounds.

Conclusions.—In this Letter, we demonstrated erasure detection for a dual-rail qubit implemented in a superconducting double-post coaxial cavity. As a result of the compact nature of this architecture, a single auxiliary transmon is sufficient for erasure detection and control of both cavity modes. We measure an average erasure rate of $3.981 \pm 0.003\ (\mathrm{ms})^{-1}$, which corresponds to 4.8% per measurement, with a false-negative rate of 0.28%. In addition, we developed a protocol to perform joint-Wigner tomography which relies on matching the dispersive interaction rates between cavity modes and transmon. From 2D cuts of the joint-Wigner function space, we reconstruct the encoded information given the outcomes of the erasure detection and extract the residual Pauli errors within the dual-rail code space. We observe that dephasing type errors dominate at a rate up to $0.170\ (\mathrm{ms})^{-1}$, 0.2% per measurement, a result expected from the finite bit-flip rate of the transmon and the mismatch in the cross-Kerr rates during the erasure detection circuit. Finally, residual bit-flip and leakage errors are negligible with an upper bound of $\sim 10^{-4}\ (\mathrm{ms})^{-1}$, highlighting a clear hierarchy of rates where erasure dominate over Pauli errors. These results, combined with the high-fidelity beam splitters recently demonstrated [33,39], suggest a promising pathway toward concatenating superconducting cavity-based dual-rail qubits within a surface code and leverage the higher threshold and favorable scaling with code distance. Finally, it should be possible to further take advantage of the high noise bias [3,40–42], of the Pauli errors in the dual-rail subspace when designing the surface code architecture to further improve upon the advantage of erasure detection.

We thank Shantanu Mundhada, Shraddha Singh, Shruti Puri, Alec Eickbusch, Patrick Winkel, and Aniket Maiti for helpful discussions and insights throughout the project. This research was supported by the U.S. Army Research Office (ARO) under Grants No. W911NF-18-1-0212 and No. W911NF-23-1-0051, by the U.S. Department of Energy, Office of Science, National Quantum Information Science Research Centers, Co-design Center for Quantum Advantage (C2QA) under Contract No. DE-SC0012704, by the Air Force Office for Scientific Research (AFOSR) under Grant No. FA9550-19-1-0399, and by the National Science Foundation (NSF) under Grant No. 2216030. Fabrication facilities use was supported by the Yale Institute for Nanoscience and Quantum Engineering (YINQE) and the Yale SEAS Cleanroom.

*These authors contributed equally to this work.
†akshay.koottandavida@yale.edu
‡ioannis.tsioutsios@yale.edu
§michel.devoret@yale.edu

[1] A. Steane, Multiple-particle interference and quantum error correction, Proc. R. Soc. A **452**, 2551 (1997).
[2] A. G. Fowler, M. Mariantoni, J. M. Martinis, and A. N. Cleland, Surface codes: Towards practical large-scale quantum computation, Phys. Rev. A **86**, 032324 (2012).
[3] J. P. Bonilla Ataides, D. K. Tuckett, S. D. Bartlett, S. T. Flammia, and B. J. Brown, The XZZX surface code, Nat. Commun. **12**, 2172 (2021).
[4] S. Krinner, N. Lacroix, A. Remm, A. Di Paolo, E. Genois, C. Leroux, C. Hellings, S. Lazar, F. Swiadek, J. Herrmann, G. J. Norris, C. K. Andersen, M. Müller, A. Blais, C. Eichler, and A. Wallraff, Realizing repeated quantum error correction in a distance-three surface code, Nature (London) **605**, 669 (2022).
[5] D. Gottesman, A. Kitaev, and J. Preskill, Encoding a qubit in an oscillator, Phys. Rev. A **64**, 012310 (2001).
[6] M. H. Michael, M. Silveri, R. T. Brierley, V. V. Albert, J. Salmilehto, L. Jiang, and S. M. Girvin, New class of

quantum error-correcting codes for a bosonic mode, Phys. Rev. X **6**, 031006 (2016).

[7] M. Mirrahimi, Z. Leghtas, V. V. Albert, S. Touzard, R. J. Schoelkopf, L. Jiang, and M. H. Devoret, Dynamically protected cat-qubits: A new paradigm for universal quantum computation, New J. Phys. **16**, 045014 (2014).

[8] V. V. Albert, S. O. Mundhada, A. Grimm, S. Touzard, M. H. Devoret, and L. Jiang, Pair-cat codes: autonomous error-correction with low-order nonlinearity, Quantum Sci. Technol. **4**, 035007 (2019).

[9] N. Ofek, A. Petrenko, R. Heeres, P. Reinhold, Z. Leghtas, B. Vlastakis, Y. Liu, L. Frunzio, S. M. Girvin, L. Jiang, M. Mirrahimi, M. H. Devoret, and R. J. Schoelkopf, Extending the lifetime of a quantum bit with error correction in superconducting circuits, Nature (London) **536**, 441 (2016).

[10] V. V. Sivak, A. Eickbusch, B. Royer, S. Singh, I. Tsioutsios, S. Ganjam, A. Miano, B. L. Brock, A. Z. Ding, L. Frunzio, S. M. Girvin, R. J. Schoelkopf, and M. H. Devoret, Real-time quantum error correction beyond break-even, Nature (London) **616**, 50 (2023).

[11] Z. Ni, S. Li, X. Deng, Y. Cai, L. Zhang, W. Wang, Z.-B. Yang, H. Yu, F. Yan, S. Liu, C.-L. Zou, L. Sun, S.-B. Zheng, Y. Xu, and D. Yu, Beating the break-even point with a discrete-variable-encoded logical qubit, Nature (London) **616**, 56 (2023).

[12] Google Quantum AI, Suppressing quantum errors by scaling a surface code logical qubit, Nature (London) **614**, 676 (2023).

[13] M. Grassl, T. Beth, and T. Pellizzari, Codes for the quantum erasure channel, Phys. Rev. A **56**, 33 (1997).

[14] Y. Wu, S. Kolkowitz, S. Puri, and J. D. Thompson, Erasure conversion for fault-tolerant quantum computing in alkaline earth Rydberg atom arrays, Nat. Commun. **13**, 4657 (2022).

[15] S. Ma, G. Liu, P. Peng, B. Zhang, S. Jandura, J. Claes, A. P. Burgers, G. Pupillo, S. Puri, and J. D. Thompson, High-fidelity gates and mid-circuit erasure conversion in an atomic qubit, Nature (London) **622**, 279 (2023).

[16] K. Sahay, J. Jin, J. Claes, J. D. Thompson, and S. Puri, High-threshold codes for neutral-atom qubits with biased erasure errors, Phys. Rev. X **13**, 041013 (2023).

[17] A. Kubica, A. Haim, Y. Vaknin, H. Levine, F. Brandão, and A. Retzker, Erasure qubits: Overcoming the ${T}{1}$ limit in superconducting circuits, Phys. Rev. X **13**, 041022 (2023).

[18] J. D. Teoh, P. Winkel, H. K. Babla, B. J. Chapman, J. Claes, S. J. de Graaf, J. W. O. Garmon, W. D. Kalfus, Y. Lu, A. Maiti, K. Sahay, N. Thakur, T. Tsunoda, S. H. Xue, L. Frunzio, S. M. Girvin, S. Puri, and R. J. Schoelkopf, Dual-rail encoding with superconducting cavities, Proc. Natl. Acad. Sci. U.S.A. **120**, e2221736120 (2023).

[19] I. L. Chuang and Y. Yamamoto, Quantum bit regeneration, Phys. Rev. Lett. **76**, 4281 (1996).

[20] E. Zakka-Bajjani, F. Nguyen, M. Lee, L. R. Vale, R. W. Simmonds, and J. Aumentado, Quantum superposition of a single microwave photon in two different 'colour' states, Nat. Phys. **7**, 599 (2011).

[21] Y.-P. Shim and C. Tahan, Semiconductor-inspired design principles for superconducting quantum computing, Nat. Commun. **7**, 11059 (2016).

[22] D. L. Campbell, Y.-P. Shim, B. Kannan, R. Winik, D. K. Kim, A. Melville, B. M. Niedzielski, J. L. Yoder, C. Tahan, S. Gustavsson, and W. D. Oliver, Universal nonadiabatic control of small-gap superconducting qubits, Phys. Rev. X **10**, 041051 (2020).

[23] H. Levine *et al.*, Demonstrating a long-coherence dual-rail erasure qubit using tunable transmons, Phys. Rev. X **14**, 011051 (2024).

[24] K. S. Chou *et al.*, Demonstrating a superconducting dual-rail cavity qubit with erasure-detected logical measurements, arXiv:2307.03169.

[25] S. Rosenblum, P. Reinhold, M. Mirrahimi, L. Jiang, L. Frunzio, and R. J. Schoelkopf, Fault-tolerant detection of a quantum error, Science **361**, 266 (2018).

[26] M. Reagor, H. Paik, G. Catelani, L. Sun, C. Axline, E. Holland, I. M. Pop, N. A. Masluk, T. Brecht, L. Frunzio, M. H. Devoret, L. Glazman, and R. J. Schoelkopf, Reaching 10 ms single photon lifetimes for superconducting aluminum cavities, Appl. Phys. Lett. **102**, 192604 (2013).

[27] J. Koch, T. M. Yu, J. Gambetta, A. A. Houck, D. I. Schuster, J. Majer, A. Blais, M. H. Devoret, S. M. Girvin, and R. J. Schoelkopf, Charge-insensitive qubit design derived from the Cooper pair box, Phys. Rev. A **76**, 042319 (2007).

[28] E. M. Purcell, H. C. Torrey, and R. V. Pound, Resonance absorption by nuclear magnetic moments in a solid, Phys. Rev. **69**, 37 (1946).

[29] N. E. Frattini, U. Vool, S. Shankar, A. Narla, K. M. Sliwa, and M. H. Devoret, 3-wave mixing Josephson dipole element, Appl. Phys. Lett. **110**, 222603 (2017).

[30] V. V. Sivak, N. E. Frattini, V. R. Joshi, A. Lingenfelter, S. Shankar, and M. H. Devoret, Kerr-free three-wave mixing in superconducting quantum circuits, Phys. Rev. Appl. **11**, 054060 (2019).

[31] See Supplemental Material at http://link.aps.org/supplemental/10.1103/PhysRevLett.132.180601 for system parameters and details about tomography.

[32] C. Wang, Y. Y. Gao, P. Reinhold, R. W. Heeres, N. Ofek, K. Chou, C. Axline, M. Reagor, J. Blumoff, K. M. Sliwa, L. Frunzio, S. M. Girvin, L. Jiang, M. Mirrahimi, M. H. Devoret, and R. J. Schoelkopf, A Schrödinger cat living in two boxes, Science **352**, 1087 (2016).

[33] B. J. Chapman, S. J. de Graaf, S. H. Xue, Y. Zhang, J. Teoh, J. C. Curtis, T. Tsunoda, A. Eickbusch, A. P. Read, A. Koottandavida, S. O. Mundhada, L. Frunzio, M. H. Devoret, S. M. Girvin, and R. J. Schoelkopf, High-on-off-ratio beam-splitter interaction for gates on bosonically encoded qubits, PRX Quantum **4**, 020355 (2023).

[34] S. Haroche and J.-M. Raimond, *Exploring the Quantum: Atoms, Cavities, and Photons* (Oxford University Press, New York, 2006).

[35] J. Gambetta, A. Blais, D. I. Schuster, A. Wallraff, L. Frunzio, J. Majer, M. H. Devoret, S. M. Girvin, and R. J. Schoelkopf, Qubit-photon interactions in a cavity: Measurement-induced dephasing and number splitting, Phys. Rev. A **74**, 042318 (2006).

[36] N. Khaneja, T. Reiss, C. Kehlet, T. Schulte-Herbrüggen, and S. J. Glaser, Optimal control of coupled spin dynamics: Design of NMR pulse sequences by gradient ascent algorithms, J. Magn. Reson. **172**, 296 (2005).

[37] R. W. Heeres, P. Reinhold, N. Ofek, L. Frunzio, L. Jiang, M. H. Devoret, and R. J. Schoelkopf, Implementing a universal gate set on a logical qubit encoded in an oscillator, Nat. Commun. **8**, 94 (2017).

[38] P. Reinhold, Ph.D. thesis, Yale University, 2019.

[39] Y. Lu, A. Maiti, J. W. O. Garmon, S. Ganjam, Y. Zhang, J. Claes, L. Frunzio, S. M. Girvin, and R. J. Schoelkopf, High-fidelity parametric beamsplitting with a parity-protected converter, Nat. Commun. **14**, 5767 (2023).

[40] D. K. Tuckett, A. S. Darmawan, C. T. Chubb, S. Bravyi, S. D. Bartlett, and S. T. Flammia, Tailoring surface codes for highly biased noise, Phys. Rev. X **9**, 041031 (2019).

[41] D. K. Tuckett, S. D. Bartlett, and S. T. Flammia, Ultrahigh error threshold for surface codes with biased noise, Phys. Rev. Lett. **120**, 050505 (2018).

[42] S. Puri, L. St-Jean, J. A. Gross, A. Grimm, N. E. Frattini, P. S. Iyer, A. Krishna, S. Touzard, L. Jiang, A. Blais, S. T. Flammia, and S. M. Girvin, Bias-preserving gates with stabilized cat qubits, Sci. Adv. **6**, eaay5901 (2020).